Title

Nanoscale strain mapping in battery nanostructures

Journal

Applied Physics Letters, 104(7)

ISSN

0003-6951

Authors

Ulvestad, A
Cho, HM
Harder, R
et al.

Publication Date

2014-02-17

DOI

10.1063/1.4866030

Peer reviewed

Nanoscale strain mapping in battery nanostructures

Cite as: Appl. Phys. Lett. **104**, 073108 (2014); https://doi.org/10.1063/1.4866030
Submitted: 13 December 2013 . Accepted: 05 February 2014 . Published Online: 19 February 2014

A. Ulvestad, H. M. Cho, R. Harder, J. W. Kim, S. H. Dietze, E. Fohtung, Y. S. Meng, and O. G. Shpyrko

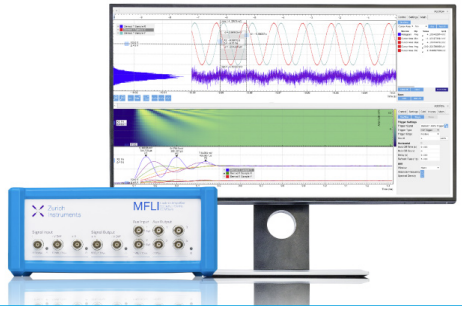

Nanoscale strain mapping in battery nanostructures

A. Ulvestad,[1,a)] H. M. Cho,[2] R. Harder,[3] J. W. Kim,[1] S. H. Dietze,[1] E. Fohtung,[4,5] Y. S. Meng,[2] and O. G. Shpyrko[1]
[1]*Department of Physics, University of California-San Diego, La Jolla, California 92093-0319, USA*
[2]*Department of NanoEngineering, University of California-San Diego, La Jolla, California 92093-0448, USA*
[3]*Advanced Photon Source, Argonne National Laboratory, Argonne, Illinois 60439, USA*
[4]*Manuel Lujan Neutron Scattering Center, Los Alamos National Laboratory, Los Alamos, New Mexico 87545, USA*
[5]*Department of Physics, New Mexico State University, Las Cruces, New Mexico 88003, USA*

(Received 13 December 2013; accepted 5 February 2014; published online 19 February 2014)

Coherent x-ray diffraction imaging is used to map the local three dimensional strain inhomogeneity and electron density distribution of two individual $LiNi_{0.5}Mn_{1.5}O_{4-\delta}$ cathode nanoparticles in both *ex-situ* and *in-situ* environments. Our reconstructed images revealed a maximum strain of 0.4%. We observed different variations in strain inhomogeneity due to multiple competing effects. The compressive/tensile component of the strain is connected to the local lithium content and, on the surface, interpreted in terms of a local Jahn-Teller distortion of Mn^{3+}. Finally, the measured strain distributions are discussed in terms of their impact on competing theoretical models of the lithiation process. © *2014 AIP Publishing LLC*. [http://dx.doi.org/10.1063/1.4866030]

The reduction of battery capacity after many charge/discharge cycles is a well known, yet poorly understood, phenomenon affecting battery performance in a wide range of devices, including cell phones, computers, and electric vehicles.[1,21,22,28] Even the ubiquitous lithium ion battery, which has several desirable properties,[26] suffers under repeated cycling.[2] A detailed understanding of the various processes thought to be involved would shed light on ways to increase longevity and maintain capacity for a larger number of cycles in both current and next generation batteries.

Possible mechanisms for the degradation of battery capacity include unwanted side reactions, electrolyte decomposition, surface film formation, active material dissolution, and structural change.[2] Lithium ions are inserted and removed from both electrodes as the battery is cycled. This causes volume expansion and contraction in a wide range of materials, including spinels, and can occur inhomogeneously, which induces strain in the active material particles.[5,14] This strain can cause irreversible cracking if it is above the threshold tensile strength of the material.[7,40,41] Cracking may lead to disconnection of some active material from the conductive matrix. Strain clearly plays a key role in battery performance and capacity retention.

Although other methods can provide globally averaged strain information,[9,25] improvements in performance will likely require understanding strain at the single particle level. Individual particle information leads, potentially, to a better understanding of how the ensemble functions. If a particular size and shape of particle exhibits minimal strain upon cycling, this can motivate improvement in synthesis techniques to produce a cathode composed of this specific particle. From a fundamental point of view, how phase transitions happen at the single particle level remains unexplored.

Spinel materials are attractive candidates for cathodes in future commercial batteries due to their specific energy, cost, availability, and electrode potential.[8,15,26] In general, the spinel structure enhances solid state lithium ion transport because it is based on a three dimensional MO_2 (M: transition metals) host. The pathway relies on vacancies in the transition metal layer along the (111) direction. In the LiM_2O_4 spinel structure, M cations occupy the octahedral site but $\frac{1}{4}$ are located in the lithium layer along the (111) direction, which leaves $\frac{1}{4}$ of the sites in the transition metal layer vacant.[34] Lithium ions then occupy the tetrahedral sites in the lithium layer, and these sites share faces with the empty octahedral sites in the metal layer.[36,37]

$LiNi_{0.5}Mn_{1.5}O_{4-\delta}$ (LNMO) is the particular type of lithium oxide spinel studied in this experiment, where $\delta \approx 0.1$ indicates the degree of disorder and the amount of oxygen vacancies. The unit cell for the disordered structure is shown in Figure 1. X-ray diffraction (XRD) data, charge-discharge curves, and differential capacity (dQ/dV) plots are included in supplementary material (Figs. 1s, 2s(a), and 2s(b), respectively).[43] XRD data demonstrate that the structural properties agree with previously published data,[17,42] while charge-discharge and differential capacity curves indicate good electrochemical performance and typical behavior.[17,42] Strain in these materials can come from a variety of sources, including inhomogeneous lithiation, Mn^{3+} ions undergoing a Jahn-Teller distortion, and the lattice mismatch induced during the structural phase transition that occurs upon cycling.[17–19] Modeling the lithiation process is typically done by considering spherical particles and assuming homogeneous lithiation across shells.[6] Unfortunately, there are not many experimentally determined strain distributions with which one can compare the model thus these assumptions are left unchallenged.

Coherent x-ray diffractive imaging (CXDI) in Bragg geometry is a powerful characterization technique for imaging local nanoscale lattice distortions.[12,13,30] CXDI is fundamentally different than other forms of microscopy. Instead of using a lens to form the image of the sample, the method

[a)]Electronic mail: aulvesta@ucsd.edu

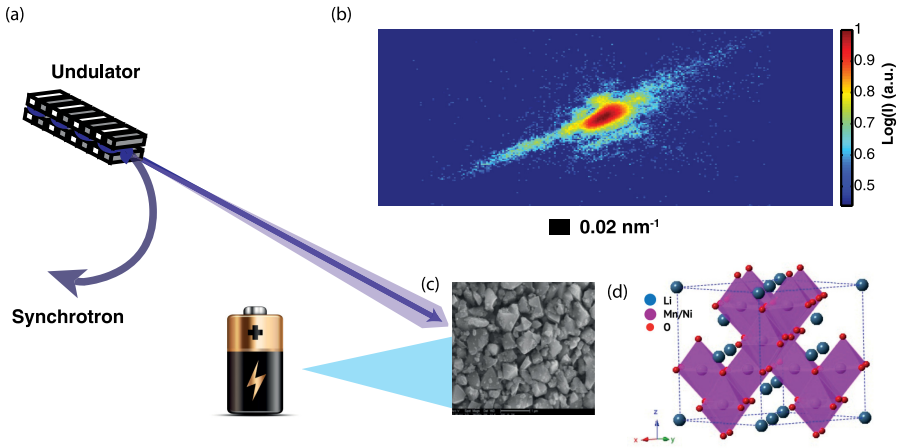

FIG. 1. (a) Coherent x-rays are produced that illuminate the sample and scatter to give (b) Coherent diffraction pattern from a particular cathode particle, (c) Electron microscopy image of the pristine cathode powder, and (d) Unit cell for the cathode material.

relies on highly coherent sources of x-rays and the remarkable sensitivity of the scattered coherent beam to the internal structure of the sample. In CXDI the coherently scattered light, or coherent diffraction pattern as shown in Figure 1, is directly measured in the far field on an area detector such as a Charge Coupled Detector (CCD). Since only the intensities of the scattered wave can be measured, and not the relative phases of the beams, computational phase retrieval algorithms are employed to generate the image.[10,11]

The strain in the sample will manifest itself in the diffraction pattern as an asymmetry of the coherent diffraction intensities around the Bragg peak of the lattice. An asymmetrical Fourier transform implies a complex real space image. The amplitude will be directly interpreted as the density distribution of the sample, while the phase can be shown to be directly related to a projection of the local lattice distortion onto the G_{hkl} vector of the Bragg peak which was measured.[4,23,24,29,30] The strain is defined as the gradient of this displacement. In principle, three independent Bragg reflections are necessary to construct the full strain tensor. In this experiment, only the (111) reflection is measured and thus only three components of the strain tensor can be computed.

The phase problem in CXDI is similar in nature to the famous phase problem of x-ray crystallography.[31] An important difference in CXDI is the ability to oversample the diffraction pattern of the sample in reciprocal space. This fact allows many more constraints to be employed in the phasing retrieval process.[10] The basic concept in phase retrieval is to iterate between real and Fourier space, using a Fast Fourier Transform (FFT), and apply the appropriate constraint in each space. In Fourier space the constraint is simple: the amplitude is set to the measured amplitude, which is the square root of the measured CCD intensity. The real space constraint depends on what algorithm is chosen. Fienup's Hybrid Input-Output (HIO)[10] and the Error Reduction (ER) algorithm were used here. This procedure is done iteratively until it converges on a solution, defined by the error metric, which consists of amplitudes and phases for both spaces.

Several checks were done on the reproducibility and robustness of the phase reconstructions. The diffraction data were centered via a sub-pixel shift to the (h,k,l) of the center of mass of the measured intensity. Each individual particle was reconstructed many times, each with a different set of random phases, and what is shown is the average of at least 5 algorithm solutions. The phase at the reconstructions center of mass is set to zero to remove any global phase offset. The Fourier space error metric, which is the sum square of the deviations of the reconstructed amplitudes from the measured, was on the order of 10^{-3}. Finally, a coordinate transformation back to the lab frame was performed to simplify computation of the compressive/tensile strain.

$LiNi_{0.5}Mn_{1.5}O_{4-\delta}$ spinel materials with the disordered structure were synthesized using the sol-gel method. The sol solution was prepared from the stoichiometric mixture of Ni(CH3COO)2·4H2O (Aldrich), Mn(CH3COO)2·4H2O (Aldrich), and LiOH·2H2O (Aldrich) in distilled water. Aqueous solution of citric acid was added drop-wise to the mixture with continuous stirring. The pH of the solution was adjusted to 7 by adding an ammonium hydroxide solution. After gel formation at 70 °C with vigorous stirring, the precursor was further dried in a vacuum oven overnight. The resulting gel precursors were decomposed at 500 °C for 12 h in air and then calcinated at 900 °C for 14 h in air. Typical morphology of the $LiNi_{0.5}Mn_{1.5}O_{4-\delta}$ spinel materials with the disordered structure are shown Figure 1. The average particle size was about 700 nm with a range of 400–1000 nm.

The experiment was performed at 34-ID-C of the Advanced Photon Source (Argonne National Laboratory). A double crystal monochromator was used to select 8.919 keV x-rays with 1 eV bandwidth, and longitudinal coherence length of about 0.7 μm. Slits were used to select a coherent fraction of the beam from the synchrotron that was then focused to about 1.0 μm^2. The pristine spinel powder was mixed with an equal volume solution of duco cement and then held in place on kapton tape for the *ex-situ* experiment (particle 1). For the *in-situ* experiment (particle 2), a modified coin cell was used that does not change the sample environment and is further detailed in Fig. 3s.[43] The CCD detector was oriented at an arbitrary (111) direction corresponding to a 2θ of $\approx 18°$. The sample was then scanned across the beam until a particle satisfying the Bragg condition illuminated the detector.

Coherent diffraction patterns were recorded for the rocking curve of the (111) Bragg reflection by rotating the sample through the Bragg condition in increments of about 0.01 deg. In our experiment, a CCD detector with 20 μm pixel size was used to collect the 2D diffraction slice for 40 slices. Full

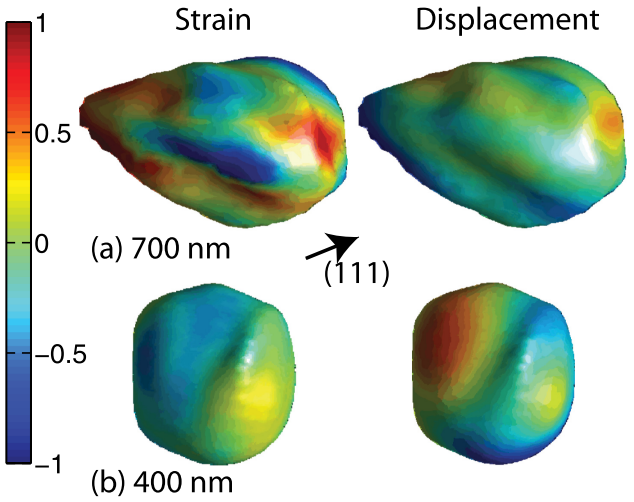

FIG. 2. Isosurface (25%) projections of strain ($\frac{\partial u_{111}}{\partial x_{111}} \times 10^3$) and displacement (in lattice units) for (a) particle 1 (*ex-situ*, pristine state) and for (b) particle 2 (*in-situ*, pristine state) at 50 nm resolution.

3D diffraction patterns were then constructed by stacking these 2D frames together.

The reconstructed real space maps of electron density, lattice displacement, and compressive/tensile strain in the (111) direction for the two different particles are shown in Figure 2. Particle 1 is approximately 700 nm in the largest dimension and imaged in an *ex-situ* environment. Particle 2 is approximately 400 nm in diameter and imaged in an *in-situ* coin cell environment. The surface is drawn by specifying a constant value of electron density at 25% of the maximum. Particle cross sections displaying the interior strain distribution are shown in Figure 3. The resolution of these maps, calculated geometrically from the maximum momentum transfer we measure and verified by computation of the phase retrieval transfer function,[4,35] is approximately 50 nanometers (nm). The root mean square strain values are displayed in Table I for the center (150 nm sphere), surface (150 nm shell), and entire particle.

The reconstructed maps provide insight into the structure and strain of pristine (fully lithiated, uncharged) $LiNi_{0.5}Mn_{1.5}O_{4-\delta}$ cathode. The origin of strain in these particles is not well understood and can come from a variety of effects. We rule out particle-particle electrochemical interaction because measurements were made at open circuit voltage (O.C.V.) in which the particles do not exchange lithium with their neighbors, or we would observe current flow. There are residual strains from the manufacturing of these particles but we expect them to be small based on our atomic resolution microscopy image which shows well aligned atomic columns.

In spinel materials, inserting lithium expands the lattice constant, while removing lithium compresses the lattice constant. Provided this is the dominating effect in the strain distribution, the compressive/tensile component of the strain then represents a map of lithium dense and lithium sparse regions. We see in Figure 2 that the strain is not homogeneous over the surface of either particle, which would support the so-called phase field models of lithium insertion[32] and not favor bulk diffusion limited "shrinking core" models.

Both particles also display differences between their strain and their displacement. Although atoms in particle 2 are displaced further from equilibrium, the overall strain is lower compared to particle 1. Differences in the particle strain distributions come from a number of effects, including size differences, sample environment differences, and shape differences. Although we cannot untangle all the effects here, the more symmetric particle (2) is less strained on the surface. Cross sections showing the interior distribution of compressive/tensile strain in particles 1 and 2 are shown in Figure 3. We see immediately that the smaller, more symmetric particle 2 is much more homogeneous in terms of strain than particle 1. Assuming, again, that lithium insertion is the dominating effect in the strain of the pristine state, we see that the particles really are inhomogeneously lithiated. These maps, as well as those in Figure 2, help us visualize the effects of size, shape, and lithium content on the strain in these cathode particles. This full three dimensional information can be used to determine, quantitatively, the amount of strain in any region.

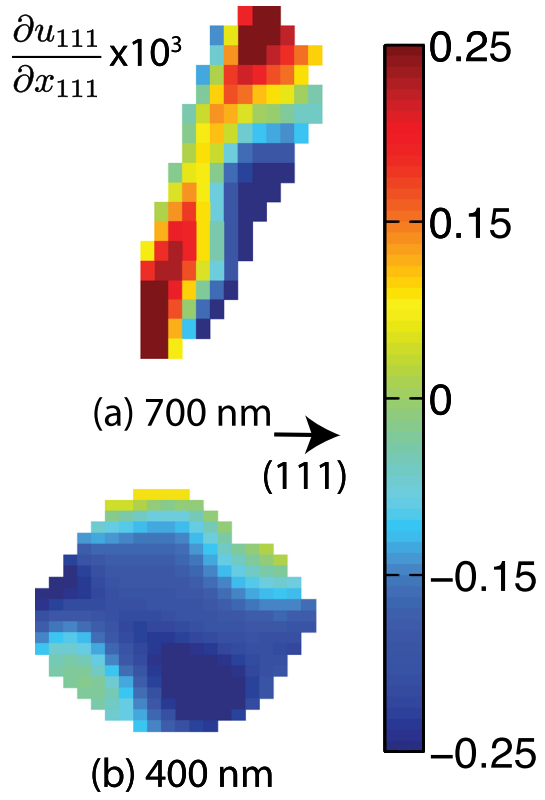

FIG. 3. Cross sections showing the interior distribution of strain in (a) particle 1 and (b) particle 2 at 50 nm resolution.

Table I shows the root mean square strain for the total particle as well as for center (150 nm sphere) and surface (150 nm shell) regions. Both particles display the same feature: surface strain is higher than central strain. We expect surface effects to be important in nano particles and we see evidence of that here. Surface strain in these particular type of particles is connected to Mn^{3+} on the surface, produced

TABLE I. Quantitative strain metrics for the two particles.

Particle	Total strain	Center strain	Surface strain
1, *ex-situ*	1.02×10^{-5}	2.21×10^{-4}	3.79×10^{-4}
2, *in-situ*	1.25×10^{-5}	1.97×10^{-4}	2.07×10^{-4}

by high calcination temperature.[27] As mentioned previously, both simulation[33] and experiment[3] point to the formation of Mn^{3+}, although through different mechanisms.

Mn^{+3} has four 3d electrons, and in a six-coordinated oxygen environment it can undergo what is known as a Jahn-Teller distortion and displace the atom from its equilibrium position.[38,39] The Jahn-Teller (JT) theorem states that in a nonlinear molecule, if degenerate orbitals are asymmetrically occupied, a distortion occurs to remove the degeneracy and lower the overall energy. Significant distortions occur in d^4 high spin ions octahedral ions, which include Mn^{+3}. Unfortunately, the JT theorem is unable to predict the magnitude of the distortion.

Equal concentrations of Mn^{+3} and Mn^{+4} are observed in $LiMn_2O_4$.[20] Introducing Nickel reduces the concentration of Mn^{+3} and improves capacity retention.[16,20] In our particular sample, we compare the measured discharge capacity to the theoretical capacity and arrive at a relative concentration of 13% Mn^{+3}. We will use this number to calculate the magnitude of the JT effect after making several other assumptions, including: the calculated compressive/tensile strain is due only to the JT effect, the strain from multiple ions acts in a collective fashion and simply adds, and the influence of other atoms in the unit cell on the JT distortion is negligible. Under these assumptions, the percent distortion along the z-direction, $\delta z/z$, is calculated to be 2.6×10^{-4}. This is very small local distortion, as compared to other collective JT distortions, such as the distortion in $KCuF_3$ which is 5.3×10^{-2}.

Electron density and (111) displacement maps were retrieved using diffraction data from pristine $LiNi_{0.5}Mn_{1.5}O_{4-\delta}$ cathode in both *ex-situ* (particle 1) and *in-situ* (particle 2) experiments at Beamline 34 ID-C at the Advanced Photon Source. We applied CXDI to a real system, and gained insight into the strain in this important class of materials. The compressive/tensile strain, which can be an indication of the local lithium concentration, was calculated from the gradient of the displacement. These strain maps call into question the assumption of homogeneity across "shells" used in theoretical models. The strain maps also demonstrate how particle shape, size, and environment can shape the strain distribution, which influences electrochemical performance. Strain inhomogeneity in single cathode particles was not documented before. The strain was quantified in terms of the root mean square, and the surface strain can be explained by Mn^{3+} that undergoes a local JT distortion. We are able to calculate the magnitude of this local distortion under a number of assumptions and compare it with a known collective JT distortion of another system.

This work was supported by U.S. Department of Energy, Office of Science, Office of Basic Energy Sciences, under Contract No. DE-SC0001805 and by the UCSD Chancellor's Interdisciplinary Award. Use of the Advanced Photon Source, an Office of Science User Facility operated for the U.S. Department of Energy (DOE) Office of Science by Argonne National Laboratory, was supported by the U.S. D.O.E. under Contract No. DE-AC02-06CH11357. The author thanks beam line scientist David Vine and staff at Argonne National Laboratory and the Advanced Photon Source. The author thanks Kyler Carrol for useful discussions regarding the properties of lithium oxide spinels.

[1]A. S. Andersson and J. O. Thomas, J. Power Sources **97**, 498–502 (2001).
[2]P. Arora, R. E. White, and M. Doyle, J. Electrochem. Soc. **145**(10), 3647–3667 (1998).
[3]J. Cabana, M. Casas-Cabanas, F. O. Omenya, N. A. Chernova, D. Zeng, M. S. Whittingham, and C. P. Grey, Chem. Mater. **24**(15), 2952–2964 (2012).
[4]H. N. Chapman, A. Barty, S. Marchesini, A. Noy, S. P. Hau-Riege, C. Cui, M. R. Howells, R. Rosen, H. He, J. C. H. Spence, U. Weierstall, T. Beetz, C. Jacobsen, and D. Shapiro, J. Opt. Soc. Am. A **23**(5), 1179–1200 (2006).
[5]Y.-T. Cheng and M. W. Verbrugge, J. Electrochem. Soc. **157**(4), A508–A516 (2010).
[6]J. Christensen and J. Newman, J. Electrochem. Soc. **153**(6), A1019–A1030 (2006).
[7]J. Christensen and J. Newman, J. Solid State Electrochem. **10**(5), 293–319 (2006).
[8]B. Dunn, H. Kamath, and J.-M. Tarascon, Science **334**(6058), 928–935 (2011).
[9]C. R. Fell, M. Chi, Y. S. Meng, and J. L. Jones, Solid State Ionics **207**, 44–49 (2012).
[10]J. R. Fienup, Appl. Opt. **21**(15), 2758–2769 (1982).
[11]J. R. Fienup, J. C. Marron, T. J. Schulz, and J. H. Seldin, Appl. Opt. **32**(10), 1747–1767 (1993).
[12]E. Fohtung, J. W. Kim, K. T. Chan, R. Harder, E. E. Fullerton, and O. G. Shpyrko, Appl. Phys. Lett. **101**(3), 033107 (2012).
[13]E. B. Fohtung, Ph.D. thesis, Universitätsbibliothek Freiburg, 2010.
[14]R. E. Garc ia, Y.-M. Chiang, W. C. Carter, P. Limthongkul, and C. M. Bishop, J. Electrochem. Soc. **152**(1), A255–A263 (2005).
[15]R. J. Gummow, A. De Kock, and M. M. Thackeray, Solid State Ionics **69**(1), 59–67 (1994).
[16]J. Yu. Huang, L. Zhong, C. M. Wang, J. P. Sullivan, W. Xu, L. Q. Zhang, S. X. Mao, N. S. Hudak, X. H. Liu, A. Subramanian, H. Fan, L. Qi, A. Kushima, and J. Li, Science **330**(6010), 1515–1520 (2010).
[17]J.-H. Kim, S.-T. Myung, C. S. Yoon, S. G. Kang, and Y.-K. Sun, Chem. Mater. **16**(5), 906–914 (2004).
[18]J.-H. Kim, C. S. Yoon, S.-T. Myung, J. Prakash, and Y.-K. Sun, Electrochem. Solid-State Lett. **7**(7), A216–A220 (2004).
[19]S. J. Leake, R. Harder, and I. K. Robinson, New J. Phys. **13**(11), 113009 (2011).
[20]X. Li, Y. Xu, and C. Wang, J. Alloys Compd. **479**(12), 310–313 (2009).
[21]S. Marchesini, H. He, H. N. Chapman, S. P. Hau-Riege, A. Noy, M. R. Howells, U. Weierstall, and J. C. H. Spence, Phys. Rev. B **68**(14), 140101 (2003).
[22]Y. Matsumura, S. Wang, and J. Mondori, J. Electrochem. Soc. **142**(9), 2914–2918 (1995).
[23]A. A. Minkevich, T. Baumbach, M. Gailhanou, and O. Thomas, Phys. Rev. B **78**, 174110 (2008).
[24]A. A. Minkevich, E. Fohtung, T. Slobodskyy, M. Riotte, D. Grigoriev, T. Metzger, A. C. Irvine, V. Novák, V. Holý, and T. Baumbach, Europhys. Lett. **94**, 66001 (2011).
[25]M. Morcrette, Y. Chabre, G. Vaughan, G. Amatucci, J.-B. Leriche, S. Patoux, C. Masquelier, and J.-M. Tarascon, Electrochim. Acta **47**(19), 3137–3149 (2002).
[26]G.-A. Nazri and G. Pistoia, *Lithium Batteries: Science and Technology* (Springer, New York, 2003), pp. 361–380.
[27]K. Ozawa, *Lithium Ion Rechargeable Batteries: Materials, Technology, and New Applications*, (Wiley, New York, 2012), pp. 11–38.
[28]D. Pavlov, J. Power Sources **42**(3), 345–363 (1993).
[29]M. A. Pfeifer, G. J. Williams, I. A. Vartanyants, R. Harder, and I. K. Robinson, Nature **442**(7098), 63–66 (2006).
[30]I. Robinson and R. Harder, Nat. Mater. **8**(4), 291–298 (2009).
[31]D. Sayre, Acta Crystallogr. **5**(6), 843 (1952).
[32]G. K. Singh, G. Ceder, and M. Z. Bazant, Electrochim. Acta **53**(26), 7599–7613 (2008).
[33]P. V. Sushko, K. M. Rosso, J.-G. Zhang, J. Liu, and M. L. Sushko, Adv. Funct. Mater. **23**, 5530 (2013).
[34]M. M. Thackeray, A. de Kock, M. H. Rossouw, D. Liles, R. Bittihn, and D. Hoge, J. Electrochem. Soc. **139**(2), 363–366 (1992).
[35]A. Tripathi, J. Mohanty, S. H. Dietze, O. G. Shpyrko, E. Shipton, E. E. Fullerton, S. S. Kim, and I. McNulty, Proc. Natl. Acad. Sci. U. S. A. **108**(33), 13393–13398 (2011).
[36]H. Wang, Y.-I. Jang, B. Huang, D. R. Sadoway, and Y.-M. Chiang, J. Electrochem. Soc. **146**(2), 473–480 (1999).

[37]B. Xu, D. Qian, Z. Wang, and Y. S. Meng, Mater. Sci. Eng., R **73**(56), 51–65 (2012).
[38]A. Yamada and M. Tanaka, Mater. Res. Bull. **30**(6), 715–721 (1995).
[39]M.-C. Yang, B. Xu, J.-H. Cheng, C.-J. Pan, B.-J. Hwang, and Y. S. Meng, Chem. Mater. **23**(11), 2832–2841 (2011).
[40]W. Yang, X. Huang, R. Harder, J. N. Clark, I. K. Robinson, and H.-K. Mao, Nat. Commun. **4**, 1680 (2013).
[41]X. Zhang, W. Shyy, and A. M. Sastry, J. Electrochem. Soc. **154**(10), A910–A916 (2007).
[42]J. Xiao, X. Chen, P. V. Sushko, M. L. Sushko, L. Kovarik, J. Feng, Z. Deng, J. Zheng, G. L. Graff, Z. Nie, D. Choi, J. Liu, J.-G. Zhang, and M. S. Whittingham, Adv. Mater. **24**(16), 2109–2116 (2012).
[43]See supplementary material at http://dx.doi.org/10.1063/1.4866030 for x-ray diffraction data, electrochemical data, and a description of the *in–situ* cell.